

**Department of Physics and Astronomy  
Heidelberg University**

Bachelor Thesis in Physics  
submitted by

**Celine Beier**

born in Dresden (Germany)

**2021**

# **Calibration of the angular analysis of $B^0 \rightarrow K^{*0}e^+e^-$ with $B^0 \rightarrow K^{*0}J/\psi(\rightarrow e^+e^-)$**

This Bachelor Thesis has been carried out by Celine Beier at the  
Physikalisches Institut Heidelberg  
under the supervision of  
Professor Dr. Ulrich Uwer

# Abstract

The rare decay  $B^0 \rightarrow K^{*0}\ell^+\ell^-$  is a flavour-changing neutral current process allowing for a test of lepton universality through the comparison of the two channels  $\ell = e, \mu$ . Currently, an angular analysis is performed for the decay  $B^0 \rightarrow K^{*0}e^+e^-$  using the data taken with the LHCb experiment in Run 1 and Run 2 with the goal of comparing the obtained angular observables to the muon channel. The decay  $B^0 \rightarrow K^{*0}J/\psi(\rightarrow e^+e^-)$  can serve as a reference for this analysis. In this thesis, an angular analysis is performed to  $B^0 \rightarrow K^{*0}J/\psi(\rightarrow e^+e^-)$  events which extracts the angular observables describing the physics of the decay. For simulated  $B^0 \rightarrow K^{*0}J/\psi(\rightarrow e^+e^-)$  decays, the obtained values match the ones used in the Monte Carlo generator which validates the event selection and fitting procedures used. Similar to the analysis of the rare decay, the angular observables for the 2016  $B^0 \rightarrow K^{*0}J/\psi(\rightarrow e^+e^-)$  data events are compared to the results published for the muon channel  $B^0 \rightarrow K^{*0}J/\psi(\rightarrow \mu^+\mu^-)$ . No significant deviation is found which confirms the analysis procedure for the rare decay  $B^0 \rightarrow K^{*0}e^+e^-$ .

# Zusammenfassung

Der seltene Zerfall  $B^0 \rightarrow K^{*0}\ell^+\ell^-$  ist ein flavour changing neutral current (Flavour-verändernder neutraler Strom)-Prozess, der über den Vergleich der beiden Zerfallskanäle  $\ell = e, \mu$  eine Möglichkeit bietet, Leptonenuniversalität zu testen. Im Moment wird der Zerfall  $B^0 \rightarrow K^{*0}e^+e^-$  mit den am LHCb-Experiment gewonnenen Daten aus Run 1 und Run 2 in Bezug auf die Zerfallswinkel untersucht mit dem Ziel, die gewonnenen Winkelobservablen mit denen des Myonen-Zerfallskanals zu vergleichen. Dafür kann der Zerfall  $B^0 \rightarrow K^{*0}J/\psi(\rightarrow e^+e^-)$  als Referenz verwendet werden. In dieser Arbeit werden für  $B^0 \rightarrow K^{*0}J/\psi(\rightarrow e^+e^-)$ -Events die Winkelobservablen, die die Physik des Zerfalls beschreiben, bestimmt. Für simulierte  $B^0 \rightarrow K^{*0}J/\psi(\rightarrow e^+e^-)$ -Zerfälle werden dabei die Werte zurückgewonnen, die in der Erzeugung der Monte Carlo-Simulation verwendet wurden, was die verwendeten Auswahl- und Fitprozesse validiert. Ähnlich zur Analyse des seltenen Zerfalls werden die Observablenwerte für die im Jahr 2016 gemessenen Zerfälle mit den publizierten Ergebnissen für den Myonen-Zerfallskanal  $B^0 \rightarrow K^{*0}J/\psi(\rightarrow \mu^+\mu^-)$  verglichen. Da kein signifikanter Unterschied gefunden wird, sind die durchgeführte Analyseschritte verifiziert.

# Contents

<b>1</b>	<b>Introduction</b>	<b>3</b>
<b>2</b>	<b>Rare Decays in the Standard Model</b>	<b>4</b>
2.1	Standard Model . . . . .	4
2.1.1	Fundamental Forces and Gauge Bosons . . . . .	4
2.1.2	Fundamental Fermions . . . . .	4
2.2	Flavour Changing Neutral Current Processes . . . . .	6
2.3	Lepton Universality . . . . .	6
2.4	$B^0 \rightarrow K^{*0} \ell^+ \ell^-$ . . . . .	6
2.4.1	Definition of the Decay Angles . . . . .	6
2.4.2	Angular Distribution . . . . .	8
2.4.3	$B^0 \rightarrow K^{*0} \ell^+ \ell^-$ at LHCb . . . . .	10
2.4.4	$B^0 \rightarrow K^{*0} J/\psi (\rightarrow \ell^+ \ell^-)$ . . . . .	10
<b>3</b>	<b>LHCb experiment</b>	<b>11</b>
3.1	LHC . . . . .	11
3.2	LHCb Detector . . . . .	11
3.2.1	Magnet . . . . .	11
3.2.2	Tracking System . . . . .	11
3.2.3	Particle Identification System . . . . .	13
3.3	LHCb Trigger System . . . . .	14
<b>4</b>	<b>Event Selection</b>	<b>15</b>
4.1	Signal Sample . . . . .	15
4.2	Background Sample . . . . .	16
4.3	Trigger Categories . . . . .	16
<b>5</b>	<b>Angular Analysis</b>	<b>18</b>
5.1	Angular Acceptance . . . . .	18
5.2	Three-Dimensional Angular Fit . . . . .	19
5.3	Mass Fit . . . . .	24
5.4	Background . . . . .	24
5.5	Four-Dimensional Fit . . . . .	26
5.5.1	Simulated $B^0 \rightarrow K^{*0} J/\psi (\rightarrow e^+ e^-)$ Events . . . . .	26
5.5.2	Measured $B^0 \rightarrow K^{*0} J/\psi (\rightarrow e^+ e^-)$ Events . . . . .	28
<b>6</b>	<b>Conclusion</b>	<b>33</b>
	<b>Bibliography</b>	<b>34</b>

# 1 Introduction

The Standard Model summarizes our current understanding of particle physics by describing all known elementary particles as well as their interaction. Despite the theory's success in the description and prediction of current experimental data, it falls short in explaining phenomena like dark matter, dark energy or baryon asymmetry which implies the existence of physics beyond the Standard Model. [1] The search for new physics is performed in two ways: On one hand, there are efforts to directly produce new particles in high-energy collisions, on the other hand, there is the search for the presence of virtual new particles influencing the decays of Standard Model particles. [2]

An example for the second approach is the investigation of the flavour-changing neutral current decay  $B^0 \rightarrow K^{*0}\ell^+\ell^-$  which only occurs via second-order loops. The resulting small branching fraction makes the decay sensitive for new physics contributions. It has been studied in regard to its branching fractions and angular observables (for example in [3, 4, 5]). Comparing those parameters for the two channels  $\ell = e$  and  $\ell = \mu$  allows for the testing of lepton universality, a property of charged leptons in the Standard Model. While the theory predicts the strengths of the electroweak interaction to be the same for electrons, muons and taus, current investigations have shown exciting tensions with the experimental results. [6]

Currently, an angular analysis for the decay  $B^0 \rightarrow K^{*0}e^+e^-$  is performed using data taken with the LHCb experiment in Run 1 and Run 2. The resulting angular observables can be compared to values measured for  $B^0 \rightarrow K^{*0}\mu^+\mu^-$  to allow for another test of lepton universality.

This thesis aims to perform an angular analysis of the decay  $B^0 \rightarrow K^{*0}(\rightarrow K^+\pi^-)J/\psi(\rightarrow e^+e^-)$  which is used as a reference channel for the  $B^0 \rightarrow K^{*0}(\rightarrow K^+\pi^-)e^+e^-$  measurements. Similarly to the analysis in the rare decay the results are compared to the muon channel  $B^0 \rightarrow K^{*0}(\rightarrow K^+\pi^-)J/\psi(\rightarrow \mu^+\mu^-)$ .

## 2 Rare Decays in the Standard Model

### 2.1 Standard Model

The Standard Model (SM) is the currently accepted theory characterising all elementary particles as well as three of the four fundamental forces, each described by a quantum field theory. The following short introduction is based on [1, 7].

#### 2.1.1 Fundamental Forces and Gauge Bosons

The strong, electromagnetic and weak force are mediated by spin 1 particles called gauge bosons. The strong interaction, described by quantum chromodynamics, is exchanged by eight gluons while the force-carrying boson for electromagnetism, characterised by quantum electrodynamics, is the photon. Electromagnetic and weak interaction can be combined within the frame of the electroweak theory. The force carriers for the weak interaction are the massive  $W^+$ ,  $W^-$  and  $Z^0$  bosons.

In order to interact via one of the three forces a particle is required to carry the corresponding charge: a colour charge (red, blue, green and the respective anti-colours) for the strong force, an electric charge for electromagnetic interactions or a weak isospin for the weak force.

The Higgs particle is the only scalar (spin 0) boson in the SM and is connected to the Higgs mechanism allowing particles to acquire mass.

Gravity is the fourth fundamental force which cannot be explained within the framework of the SM yet.

#### 2.1.2 Fundamental Fermions

The 12 spin  $\frac{1}{2}$  fermions in the SM can be separated into three generations (table 1) with the corresponding particles of each generation differing from each other in their respective masses. Each generation includes two quarks and two leptons, a charged lepton (electron, muon, tau) and a neutrino.

For every fundamental fermion exists an anti-particle. Particle and anti-particle have the same mass and lifetime, but hold opposite charges.

All fermions carry a weak isospin and can therefore interact via the weak force. The three charged leptons and six quarks additionally hold an electric charge while only quarks carry a colour charge. Quarks are never observed as single particles but only in colour-neutral composites called hadrons. A meson is a hadron composed of a quark and an anti-quark whereas a baryon consists of three quarks.

	First Generation		Second Generation		Third Generation	
	Quarks					
particle	up $u$	down $d$	charm $c$	strange $s$	top $t$	beauty $b$
electric charge	$\frac{+2}{3}e$	$\frac{-1}{3}e$	$\frac{+2}{3}e$	$\frac{-1}{3}e$	$\frac{+2}{3}e$	$\frac{-1}{3}e$
mass	$2.16^{+0.49}_{-0.26} MeV$	$4.67^{+0.48}_{-0.17} MeV$	$1.27^{+0.02}_{-0.02} GeV$	$93^{+11}_{-5} MeV$	$172.8^{+0.3}_{-0.3} GeV$	$4.18^{+0.03}_{-0.02} GeV$
	Leptons					
particle	electron $e^-$	electron neutrino $\nu_e$	muon $\mu^-$	muon neutrino $\nu_\mu$	tau neutrino $\nu_\tau$	tau neutrino $\nu_\tau$
electric charge	$-1e$	$0e$	$-1e$	$0e$	$-1e$	$0e$
mass	$0.511 MeV$	$< 1.1 eV$	$106 MeV$	$< 1.1 eV$	$1776.86^{+0.12}_{-0.12} MeV$	$< 1.1 eV$

57

Table 1: Fundamental Fermions in the Standard Model. The neutrino masses are determined with a confidence level of 90%, the uncertainties for the  $e^-$  and  $\mu^-$  masses are below  $10^{-6}\%$  each. Data taken from [8].

## 2.2 Flavour Changing Neutral Current Processes

The weak interaction is the only force allowing the change of particle flavour. At tree level, flavour changing decays can only be mediated by a  $W^+$  or  $W^-$  boson and the electric charge will change alongside the particle flavour as the boson involved also carries electric charge. A process changing the particle flavour without changing the electric charge is called a flavour changing neutral current (FCNC) process. In the SM, FCNC processes do not occur at the tree-level but only in higher order interactions and accordingly, the branching fractions of processes involving FCNC decays are relatively small as there is no dominant first-order contribution. These rare decays might be sensitive to new physics (NP) beyond the SM since the magnitude of the branching fractions is similar to the one expected from NP. [6]

## 2.3 Lepton Universality

The SM predicts the particle mass to be the only difference between corresponding particles of the three generations. In particular, the electroweak coupling of charged leptons is expected to be independent of the particle flavour which is known as lepton universality. Experimentally observed deviations from lepton universality would indicate the presence of NP in the investigated process. As contributions beyond the SM in the form of virtual particles could change the branching ratio or the angular distribution of the final state particles, lepton universality is tested by comparing the same observables for decays differing only by the involved lepton. [2]

## 2.4 $B^0 \rightarrow K^{*0} \ell^+ \ell^-$

The decay  $B^0 \rightarrow K^{*0} \ell^+ \ell^-$  is a FCNC process involving a  $\bar{b} \rightarrow \bar{s}$  quark transition. The SM diagrams involved are shown in figure 1.

### 2.4.1 Definition of the Decay Angles

The kinematics of the decay  $B^0 \rightarrow K^{*0}(\rightarrow K^+ \pi^-) \ell^+ \ell^-$  can be described by  $q^2$ , the invariant mass squared of the two leptons, and the three angles  $\theta_\ell$ ,  $\theta_K$ ,  $\phi$  shown in figure 2.  $\theta_\ell$  is defined as the angle in the dilepton rest frame between the electrically positively charged lepton (positron or  $\mu^+$ ) and the dilepton flight direction,  $\theta_K$  describes the angle between the  $K^{*0}$  flight direction and the kaon in the  $K^{*0}$  rest frame and  $\phi$  denotes the angle between the decay plane of the  $K^{*0}$  and the plane of the dileptons. [9]

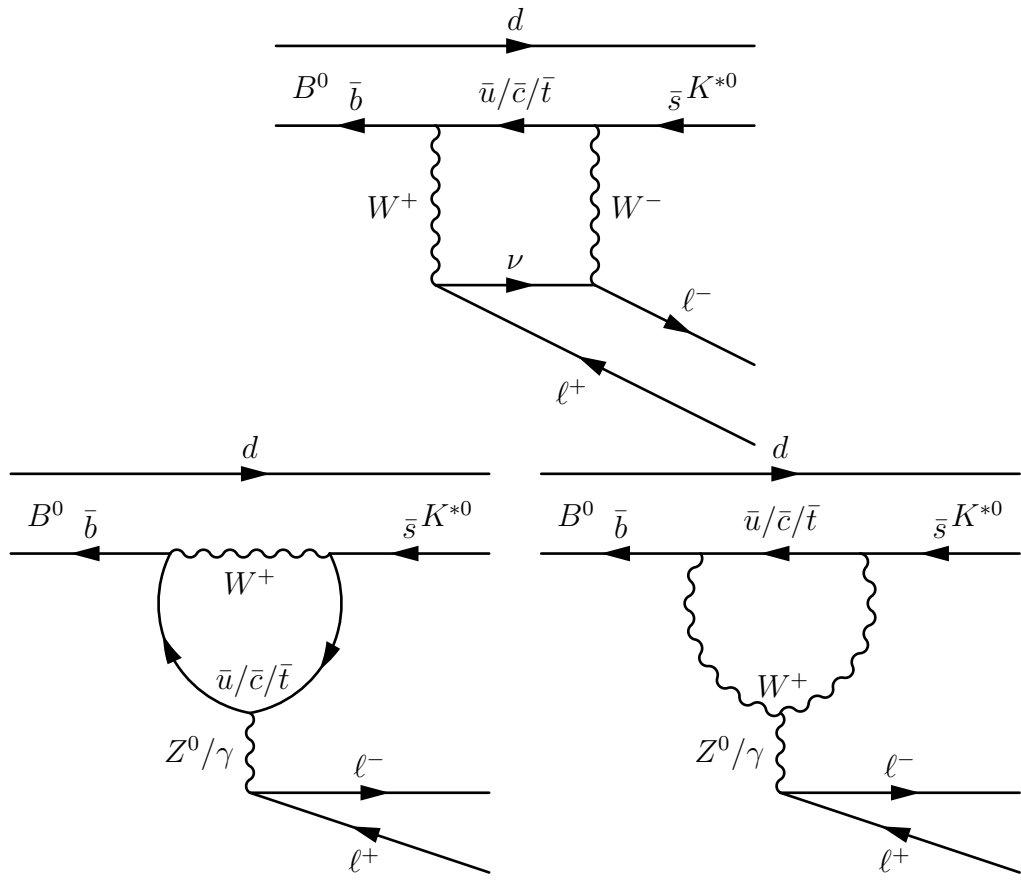


Figure 1: Feynman diagrams for the SM decay of  $B^0 \rightarrow K^{*0} \ell^+ \ell^-$  through a box (top) and an electroweak penguin (bottom) diagram. Adapted from [6].

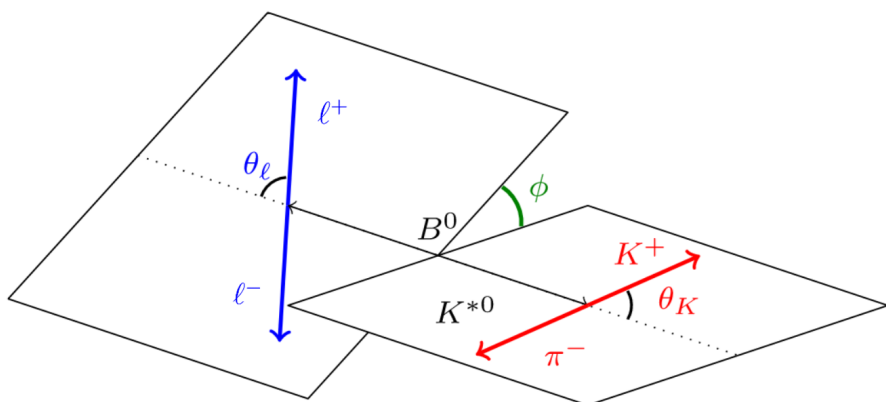


Figure 2: Definition of the three angles  $\theta_\ell$ ,  $\theta_K$ ,  $\phi$  for the decay  $B^0 \rightarrow K^{*0} \ell^+ \ell^-$ . Adapted from [4]

### 2.4.2 Angular Distribution

The decay rate  $\Gamma$  is used to describe the distribution of  $B^0 \rightarrow K^{*0}\ell^+\ell^-$  with respect to  $q^2$  and the three angles. A full derivation can be found in [9, 5]. Under the assumption of massless leptons, the differential decay rate of  $B^0 \rightarrow K^{*0}\ell^+\ell^-$  is given by

$$\begin{aligned} \frac{d^4\Gamma(B^0 \rightarrow K^{*0}\ell^+\ell^-)}{dq^2 d\cos\theta_\ell d\cos\theta_K d\phi} = & \frac{9}{32\pi} [I_1^s \sin^2\theta_K + I_1^c \cos^2\theta_K \\ & + (I_2^s \sin^2\theta_K + I_2^c \cos^2\theta_K) \cos 2\theta_\ell \\ & + I_3 \sin^2\theta_K \sin^2\theta_\ell \cos 2\phi + I_4 \sin 2\theta_\ell \sin 2\theta_\ell \cos\phi \quad (2.1) \\ & + I_5 \sin 2\theta_K \sin\theta_\ell \cos\phi + I_6 \sin^2\theta_K \cos\theta_\ell \\ & + I_7 \sin 2\theta_K \sin\theta_\ell \sin\phi + I_8 \sin 2\theta_K \sin 2\theta_\ell \sin\phi \\ & + I_9 \sin^2\theta_K \sin^2\theta_\ell \sin 2\phi ] \end{aligned}$$

The coefficients  $I_i$  are  $q^2$ -dependent angular observables including the polarization amplitudes of the final state particles. Combining the decay rates of  $B^0 \rightarrow K^{*0}(\rightarrow K^+\pi^-)\ell^+\ell^-$  and the CP-conjugated decay  $\bar{B}^0 \rightarrow \bar{K}^{*0}(\rightarrow K^-\pi^+)\ell^+\ell^-$  allows to transform the angular observables into 11 CP-asymmetries and 11 CP-averaged coefficients (S observables):

$$S_i = \frac{(I_i + \bar{I}_i)}{\frac{d\Gamma}{dq^2} + \frac{d\bar{\Gamma}}{dq^2}} \quad (2.2)$$

Only 8 S observables are independent of each other, so the angular decay distribution of the CP-averaged decay can be described using  $S_1^c, S_3, S_4, S_5, S_6, S_7, S_8, S_9$ . The  $S_1^c$  parameter describes the fraction of longitudinal polarisation of the  $K^{*0}$  meson and is therefore often labelled  $F_L$ .  $S_6$  is proportional to the asymmetry of the forward and backward flying leptons with respect to the  $B^0$  flight direction in the dilepton rest frame. It is often called the forward-backward asymmetry  $A_{FB}$ :

$$A_{FB} = \frac{3}{4} S_6 \quad (2.3)$$

Together the CP-averaged angular distribution with the S-observables is given by:

$$\begin{aligned} \frac{1}{d(\Gamma + \bar{\Gamma})/dq^2} \frac{d^4(\Gamma + \bar{\Gamma})}{dq^2 d \cos \theta_\ell d \cos \theta_K d\phi} \Big|_P = & \frac{9}{32\pi} \left[ \frac{3}{4}(1 - F_L) \sin^2 \theta_k + F_L \cos^2 \theta_k \right. \\ & + \frac{1}{4}(1 - F_L) \sin^2 \theta_k \cos 2\theta_l - F_L \cos^2 \theta_k \cos 2\theta_l \\ & + S_3 \sin^2 \theta_k \sin^2 \theta_l \cos 2\phi + S_4 \sin 2\theta_k \sin 2\theta_l \cos \phi \\ & + S_5 \sin 2\theta_k \sin \theta_l \cos \phi + \frac{4}{3} A_{FB} \sin^2 \theta_k \cos \theta_l \\ & + S_7 \sin 2\theta_k \sin \theta_l \sin \phi + S_8 \sin 2\theta_k \sin 2\theta_l \sin \phi \\ & \left. + S_9 \sin^2 \theta_k \sin^2 \theta_l \sin 2\phi \right] \end{aligned} \quad (2.4)$$

Since in  $B^0 \rightarrow K^{*0} (\rightarrow K^+ \pi^-) \ell^+ \ell^-$  the kaon and pion are coming from the  $K^{*0}$  spin 1 meson, their system has an angular momentum of 1, which is described by a so-called P-wave. However, the experimentally detected kaons and pions will also stem from random background as well as from  $B^0$  meson decays into the final state  $K^+ \pi^- \ell^+ \ell^-$  without a  $K^{*0}$  intermediate resonance. Those particles can be described by an S-wave contribution to the decay with the fraction  $F_S$ :

$$\frac{1}{d(\Gamma + \bar{\Gamma})/dq^2} \frac{d^4(\Gamma + \bar{\Gamma})}{dq^2 d \cos \theta_\ell d \cos \theta_K d\phi} \Big|_S = \frac{3}{16\pi} F_S \sin^2 \theta_\ell \quad (2.5)$$

P- and S-wave contributions to the same final state cause interference terms that have to be included for a full angular description:

$$\begin{aligned} \frac{1}{d(\Gamma + \bar{\Gamma})/dq^2} \frac{d^4(\Gamma + \bar{\Gamma})}{dq^2 d \cos \theta_\ell d \cos \theta_K d\phi} \Big|_{P+S} = & (1 - F_S) \frac{1}{d(\Gamma + \bar{\Gamma})/dq^2} \frac{d^4(\Gamma + \bar{\Gamma})}{dq^2 d \cos \theta_\ell d \cos \theta_K d\phi} \Big|_P \\ & + \frac{1}{d(\Gamma + \bar{\Gamma})/dq^2} \frac{d^4(\Gamma + \bar{\Gamma})}{dq^2 d \cos \theta_\ell d \cos \theta_K d\phi} \Big|_S \\ & + \frac{9}{32\pi} (S_{P+S1} + S_{P+S2} \cos 2\theta_\ell) \cos \theta_K \\ & + \frac{9}{32\pi} (S_{P+S3} \sin 2\theta_\ell + S_{P+S4} \sin \theta_\ell) \sin \theta_K \cos \phi \\ & + \frac{9}{32\pi} (S_{P+S5} \sin \theta_\ell + S_{P+S6} \sin 2\theta_\ell) \sin \theta_K \sin \phi \end{aligned} \quad (2.6)$$

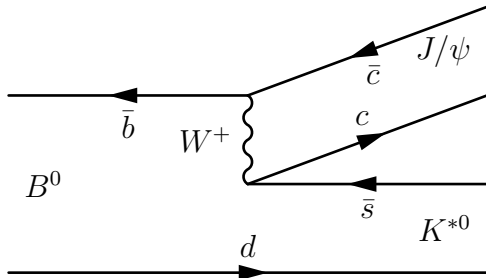


Figure 3: Feynman diagram for  $B^0 \rightarrow K^{*0} J/\psi$ . Adapted from [10].

#### 2.4.3 $B^0 \rightarrow K^{*0}\ell^+\ell^-$ at LHCb

The decay  $B^0 \rightarrow K^{*0}\ell^+\ell^-$  is investigated for the final state leptons  $\ell = e, \mu$  with regard to the branching fraction, the angular distribution and to test lepton universality in the Belle, BaBar and LHCb experiments. [2]

In the LHCb experiment, the branching fractions of the electron and muon channel are measured in [6]. An angular analysis for the muon channel is performed in [5] while for  $B^0 \rightarrow K^{*0}e^+e^-$  an angular analysis is so far only performed for the very low  $q^2$  region in [3].

#### 2.4.4 $B^0 \rightarrow K^{*0}J/\psi(\rightarrow \ell^+\ell^-)$

The decay  $B^0 \rightarrow K^{*0}J/\psi(\rightarrow \ell^+\ell^-)$  is a SM decay (figure 3) used as a reference channel for the analysis of  $B^0 \rightarrow K^{*0}\ell^+\ell^-$  as it has the same final state. In contrast to  $B^0 \rightarrow K^{*0}\ell^+\ell^-$  it can be described by only three angles  $\theta_\ell$ ,  $\theta_K$  and  $\phi$  since  $q^2$  is fixed to the  $J/\psi$  mass. The left and right handed polarisation amplitudes of the final state particles are the same which means that the S-observables  $S_5$  and  $S_7$  as well as the forward-backward asymmetry  $A_{FB}$  equal 0. The polarisation amplitudes describing the decay have been measured in [10] for the muon channel.

## 3 LHCb experiment

### 3.1 LHC

The Large Hadron Collider (LHC) at CERN near Geneva is the world's largest and most powerful particle accelerator. It provides proton-proton collisions as well as collisions involving heavy ions to eight different experiments with detectors arranged around four beam interaction points. [11]

The LHC started collecting data for physics analysis in 2011 with a beam energy of  $3.5\text{TeV}$  resulting in a center-of-mass-energy of  $\sqrt{s} = 7\text{TeV}$ . In 2012, the beam energy was increased to  $4\text{TeV}$  corresponding to  $\sqrt{s} = 8\text{TeV}$ . [12] The LHC operation in 2011 - 2012 is called Run 1 and was followed by a 2-year shutdown to upgrade the accelerator and experiments. The LHC was operating in Run 2 from 2015-2018 with a beam energy of  $6.5\text{TeV}$  resulting in  $\sqrt{s} = 13\text{TeV}$ . [13] Currently, the LHC is undergoing a second shutdown allowing for further improvements of the machines and detectors before starting into Run 3. Recommission is planned for 2021 with a beam energy of  $7\text{TeV}$  allowing for  $\sqrt{s} = 14\text{TeV}$ . [14]

### 3.2 LHCb Detector

The LHCb experiment at the LHC is dedicated to the search for new physics in CP violations and rare decays of beauty and charm hadrons produced in particle collisions. The detector components are aranged around the interaction region and beamline to allow for the detection of particles with a pseudorapidity of  $1.6 < \eta < 4.9$ . [15] Figure 4 shows the detector layout. In the following, the individual components will be discussed in greater detail, based on [15].

#### 3.2.1 Magnet

A dipol magnet is used to gain information on the the momentum of charged particles through the bending of tracks due to the Lorentz force inside the magnetic field. During data acquisition, the polarity of the electromagnet is regularly reversed to eliminate detection asymmetries arising due to the separation of oppositely charged particles.

#### 3.2.2 Tracking System

The tracking system comprises the Vertex Locator (VELO) around the proton-proton collision area, the TT as well as the T1-T3 detectors. The information

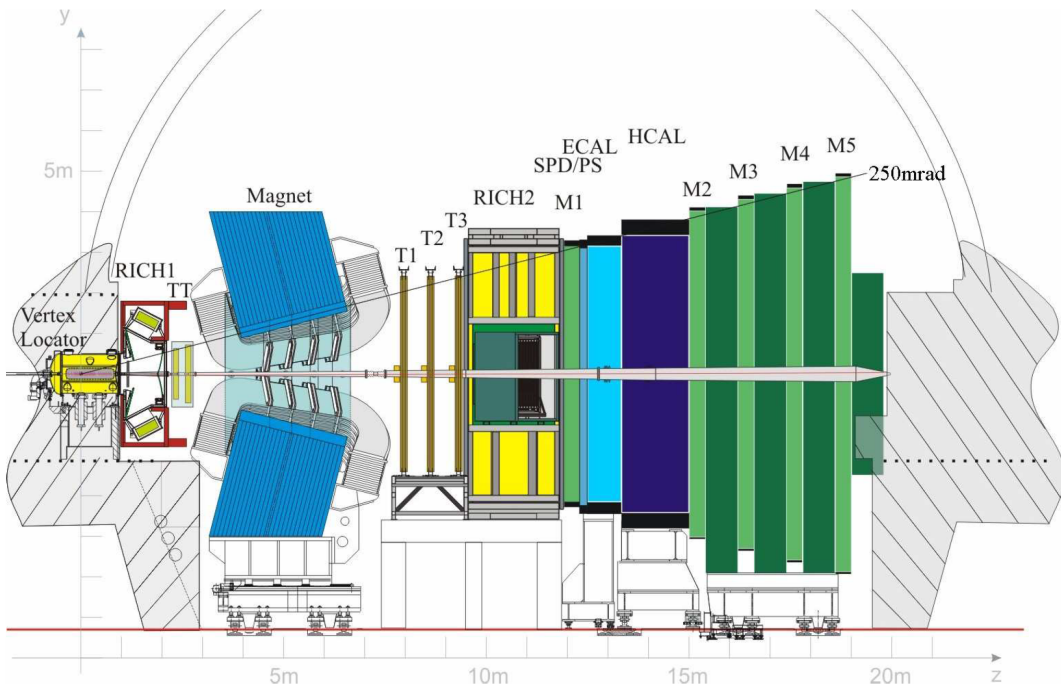


Figure 4: Cross section of the LHCb detector. From [15]

acquired from those subsystems can be combined to reconstruct the trajectories of charged particles through the detector.

The VELO consists of 42 semicircular silicon detectors providing coordinates of passing particles. It allows for the tracking of particle trajectories near the  $pp$  interaction region and the reconstruction of primary vertices from the particle collision as well as secondary vertices created by particle decays. The detector components are installed in a vacuum in order to minimize particle interaction with matter other than the semiconductor material.

The Tracker Turicensis (TT) is made out of two-layered silicon strip sensors allowing for the detection of the particle position upstream of the magnet. The tracking detectors T1-T3 are positioned downstream of the magnet and complement the TT by recording the particle coordinates after its trajectory has been bent by the magnetic field. The inner compartments close to the beam line of T1-T3 are built from multi-layered silicon strip sensors whereas the outer parts of the T1-T3 detectors are straw chambers using the ionisation of a counting gas to track passing particles. The combined tracking system has a momentum resolution of  $\Delta p/p$  of 0.35% at  $5\text{GeV}/c$  which is increasing to 0.55% for particles with a momentum larger than  $100\text{GeV}/c$ .

### 3.2.3 Particle Identification System

Particles inside the LHCb detector can be identified using the information gained from the two Ring Imaging Cherenkov counters (RICH1 and RICH2), the calorimeters (ECAL and HCAL) and the muon system (M1-M5).

The RICH1 detector is located downstream of the VELO and used for identifying particles with low momenta between  $1 - 60\text{GeV}/c$  whereas the RICH2 system further downstream covers high momenta  $> 15\text{GeV}/c$ . Both systems rely on the detection of Cherenkov light emitted by particles passing through a radiator gas with velocities above the speed of light in the respective medium. The light emission angle is proportional to the particle velocity and can be used for calculating the particle mass when combined with the refractive index of the gas and the momentum determined by the tracking system.

Located upstream of the calorimeters is a scintillator pad detector (SPD) responsive to the penetration by an electrically charged particle. The SPD and the preshower detector (PS) enclose a lead absorber where high-energy electrons, positrons or photons will start an electromagnetic shower by interacting with the absorber material. The electromagnetic shower will be registered by the PS, a scintillating detector. The electromagnetic calorimeter (ECAL) consists of alternating layers of lead and scintillator detectors whereas the hadronic calorimeter (HCAL) adapts iron as the absorbing material. ECAL and HCAL provide the particle energy and position as well as qualitative information used for particle identification.

Before reaching the calorimeter, electrons will lose energy in the form of bremsstrahlung due to their interaction with matter. When bremsstrahlung is emitted after the electron passed the magnet the photons will register in the ECAL in the same position as the electrons and the emission of bremsstrahlung will not affect the measurement of the electron energy. However, if bremsstrahlung is emitted before the electron trajectory is bent by the magnet, the bremsstrahlungs photons will form a separate cluster in the ECAL as their track is not influenced by the magnetic field. For the bremsstrahlungs recovery, photon signals in the ECAL matching the extrapolated trajectory of the electron before the magnet with an energy  $> 75\text{MeV}$  will be added to the energy of the electron to yield the initial electron energy. [6]

The muon system consists of five rectangular arrangements of a total of 1380 multi-wire proportional chambers separated by iron absorbers with the exemption of the M1 compartment close to the beam line composed of triple gas electron multiplier (triple-GEM) detectors. Both detection techniques rely on the ionisation of gas by passing muons to provide particle position and momentum.

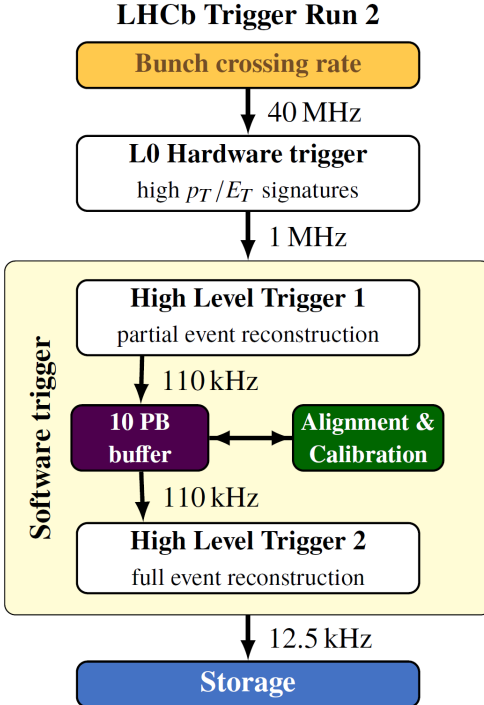


Figure 5: Schematic of the LHCb trigger system after the redesign for Run 2. From [13]

### 3.3 LHCb Trigger System

The LHCb trigger system selects the events stored for data analysis. Following the LHC Run 1 it was redesigned for Run 2 to allow for a better selection of charm and strange hadron decays as well as a full online reconstruction of the events. [13] The trigger process is illustrated in figure 5 and described in detail in [13, 15].

The first trigger stage is the hardware Level 0 (L0) trigger which reduces the LHC bunch crossing rate of 40MHz to about 1MHz. Using information of SPD, PS, ECAL, HCAL and the muon system the L0 trigger selects events producing hadrons, leptons or photons with a relative large transverse momentum or transverse energy characteristic for the decays of mesons and baryons with heavy valence quarks. The LHCb detector is only read out for the events that pass the first trigger which are then passed to the second trigger stage, the High Level Trigger (HLT). The HLT is a software trigger with the two components HLT1 and HLT2. Based on a partial reconstruction the HLT1 system performs an event selection, then the detector is calibrated and aligned, before the HLT2 performs a full event reconstruction. The events passing the trigger system are stored for analysis, the combined trigger system reduces the event rate to 12.5kHz.

Preselection Flag	Summary of the applied cuts
GenericPresel	particle identification, track quality, ghost probability, momentum cuts
MeerkatPresel	particle identification for $K, e^-, e^+$
VetoesPresel	vetoes against particle misidentification
PIDPresel	particle identification based on a trained neural network
TighterKst0Presel	restricts the reconstructed $K^{*0}$ mass
TriggerPresel	cuts based on the trigger lines for L0, HLT1 and HLT2
CloneVeto	ensures that the same track is not reconstructed twice

Table 2: Applied preselection flags implemented in the Ntuples with a short description of the corresponding cuts. Details can be found in [19].

## 4 Event Selection

This thesis uses the  $B^0 \rightarrow K^{*0} J/\psi(\rightarrow e^+e^-)$  events collected by the LHCb experiment in 2016, the corresponding Monte Carlo (MC) simulated events as well as the 2016  $B^0 \rightarrow K^{*0} e^+e^-$  phase space Monte Carlo simulation. The following section describes the selection process of the events and is based on [16, 17].

The full LHCb data set is fragmented into smaller files to allow for specific analyses by applying loose selection cuts, for example on the decay vertices, particle energies and momenta. This process is called stripping, the stripping line used to select  $B^0 \rightarrow K^{*0} J/\psi(\rightarrow e^+e^-)$  events is *Bu2LLK\_eeLine2*. The full documentation can be found in [18]. After the stripping, the reconstructed events are stored in Ntuples containing all measured and calculated variables for the event.

### 4.1 Signal Sample

To help select the signal events, a preselection is applied using flags implemented in the Ntuples which are summarising certain selection criteria. The used preselection flags are listed in table 2 together with a short description of the cuts, the full documentation can be found in [19].

To further separate the background from the signal a multivariant analysis (MVA) classifier is used. Relying on training events a machine learning system assigns MVA scores to the events which can be used to classify them as background or signal. Details on the MVA classifier are described in [20]. For this analysis, a cut on the MVA output score with

$$n_{MVA} > 0.99 \quad (4.1)$$

is applied. In addition, the  $B^0$  meson mass is calculated using a primary vertex and a  $J/\psi$  mass constraint. The following cut is applied:

$$5150 \frac{MeV}{c^2} < m_{B^0} < 5600 \frac{MeV}{c^2} \quad (4.2)$$

The  $J/\psi$  mass region is selected by a cut on  $q^2$ , the invariant dilepton mass:

$$6 \frac{(GeV)^2}{c^4} < q^2 < 11 \frac{(GeV)^2}{c^4} \quad (4.3)$$

Those selections using the preselection flags, the MVA classifier, the primary vertex and  $J/\psi$  mass constrained  $B^0$  mass as well as the  $q^2$ -cut are applied to the simulated events as well as the measured data. In addition, the simulation samples are truth-matched: The simulated events of  $B^0 \rightarrow K^{*0}J/\psi(\rightarrow e^+e^-)$  and  $B^0 \rightarrow K^{*0}e^+e^-$  contain only signal decays. However, as the events pass through the same reconstruction algorithm as the data events, misidentifications and misreconstructions occur. Simulated events with an incorrect reconstruction are sorted out, which is called truth-matching. For the simulated  $B^0 \rightarrow K^{*0}J/\psi(\rightarrow e^+e^-)$  decays the events are required to be in background category 0, 50 or 60 while for  $B^0 \rightarrow K^{*0}e^+e^-$  events have to be in background category 10, 50 or 60 to select the  $B^0 \rightarrow K^{*0}J/\psi(\rightarrow e^+e^-)$  events.

## 4.2 Background Sample

For modeling the background so-called high-mass side-band data is used. These are data events with a reconstructed  $B^0$  meson mass higher than  $5600 \frac{MeV}{c^2}$  which lie outside of the  $B^0 \rightarrow K^{*0}J/\psi(\rightarrow e^+e^-)$  signal region. To define the high-mass side-band the following cuts are used: The same preselection flags and the  $q^2$ -cut as used above for the signal selection are applied. The MVA classifier output cut is set to

$$n_{MVA} > 0.2 \quad (4.4)$$

while the primary vertex and  $J/\psi$  mass constrained  $B^0$  meson mass is cut at

$$m_{B^0} > 5600 \frac{MeV}{c^2} \quad (4.5)$$

## 4.3 Trigger Categories

The analysis of events is done in two trigger categories according to the cause of the hardware Level 0 (L0) triggering. Splitting the analysis into trigger categories helps

with taking into account different detector acceptances as well as differences between the data and MC simulation regarding the trigger category fractions. Events are sorted into  $L0E$  when an electron triggers the read out of the detector and the electron energy is above the threshold energy of  $2700\text{MeV}$ . Events in the  $L0I$  category are triggered by a particle other than the particles in the  $B^0 \rightarrow K^{*0}J/\psi(\rightarrow e^+e^-)$  decay. The two categories are exclusive as events that trigger both trigger lines are sorted into  $L0I$ .

## 5 Angular Analysis

The following angular analysis aims to fit the angular distribution of the  $B^0 \rightarrow K^{*0}J/\psi(\rightarrow e^+e^-)$  decay and extract the S-observables. The S-observables can be compared to the values measured in the angular analysis of  $B^0 \rightarrow K^{*0}J/\psi(\rightarrow \mu^+\mu^-)$  in [10] and allow for a validation of the fitting procedure intended to be used for the analysis of the rare decay  $B^0 \rightarrow K^{*0}e^+e^-$ . The analysis follows the angular analysis performed for the  $B^0 \rightarrow K^{*0}e^+e^-$  decay in the low  $q^2$ - region in [3]. It relies on adapted scripts written for the  $B^0 \rightarrow K^{*0}e^+e^-$  events which can be found in [21]. The angular distribution of the decay  $B^0 \rightarrow K^{*0}J/\psi(\rightarrow e^+e^-)$  is distorted through the detection and reconstruction processes. To include those effects into the analysis an angular acceptance function is calculated in section 5.1. Following, a three-dimensional fit over the three decay angles is done in section 5.2.

An additional change in the angular distribution is caused by background events which have passed the applied event selection as decays other than the signal  $B^0 \rightarrow K^{*0}J/\psi(\rightarrow e^+e^-)$  decay have different angular shapes. This effect can be included in the analysis through a separate fit to the background events. Signal and background events can be distinguished in the mass dimension, signal events will fit into the shape of the  $B^0$  meson mass peak while background events will be primarily in the high-mass side-band. A one-dimensional fit to the  $B^0$  meson mass calculated with a vertex and  $J/\psi$  mass constraint is done in section 5.3. The background from the high-mass side-band sample from section 4.2 is studied in section 5.4.

The full angular fit to the three decay angles including the calculated acceptance, a mass fit to distinguish signal and background as well as the modeling of the background events is then done in section 5.5.

### 5.1 Angular Acceptance

The angular distribution of a decay can be distorted by the geometry of the detector as well as the event reconstruction and selection processes. These effects must be included into the angular fit by multiplying the angular probability density function (PDF) with an angular acceptance function.

To calculate an acceptance function,  $B^0 \rightarrow K^{*0}e^+e^-$  events are simulated without underlying physics and only momentum conservation. This yields an uncorrelated flat distribution in all three angles, which is called a phase space distribution. The events are passed through a detector simulation as well as the reconstruction and selection processes. The resulting angular distributions are used to gain the acceptance by comparing them to the original flat distributions. In a three-dimensional

histogram of the events the acceptance for each bin is defined as: [17]

$$\epsilon = \frac{N_{\text{reconstructed}}}{N_{\text{generated}}} \quad (5.1)$$

Instead of using the three-dimensional histogram to include the acceptance into the angular fits, the acceptance is modelled by a polynomial expansion using Legendre polynomials. A polynomial expansion of the acceptance function takes into account that the acceptance is expected to vary smoothly and not discretely with the bins used in the histograms. Legendre-polynomials are used as different orders are orthonormal to each other with regard to the integration between  $-1$  and  $1$  and therefore the correlation between the individual Legendre coefficients is minimal. [17] For the  $\cos \theta_\ell$ - dimension the Legendre polynomials are truncated at order 6 while for  $\cos \theta_K$  and  $\phi$  polynomials up to the order 8 are included. The acceptance function in the two trigger categories is obtained through a three-dimensional fit over the angles using a method of moments calculation. Projections of the three-dimensional acceptance function into the dimensions of the three angles are shown in figure 6.

This fit of the detector acceptance is tested by reweighting the  $B^0 \rightarrow K^{*0} e^+ e^-$  phase space MC events with the inverse of the acceptance function. In figure 7 and figure 8 the events are plotted in two-dimensional histograms of two angles each. While the unweighted events show a highly irregular distribution resulting from the distortion of the flat distributions by acceptance effects, the reweighted events are significantly flatter. The reweighting is reversing the acceptance effects and yields the initial flat angular distribution. This validates the acceptance fit.

## 5.2 Three-Dimensional Angular Fit

The simulated  $B^0 \rightarrow K^{*0} J/\psi (\rightarrow e^+ e^-)$  events do not include a S-wave contribution but only P-wave signal events. The angular PDF can therefore be obtained by multiplying the angular distribution described by equation 2.4 with the angular acceptance function. This function is fitted to the angular distribution of the simulated  $B^0 \rightarrow K^{*0} J/\psi (\rightarrow e^+ e^-)$  events using a three-dimensional unbinned maximum likelihood fit. The fit is done in trigger categories. Figure 9 shows projections of the fitted angular PDF in the three dimensions of the angles.

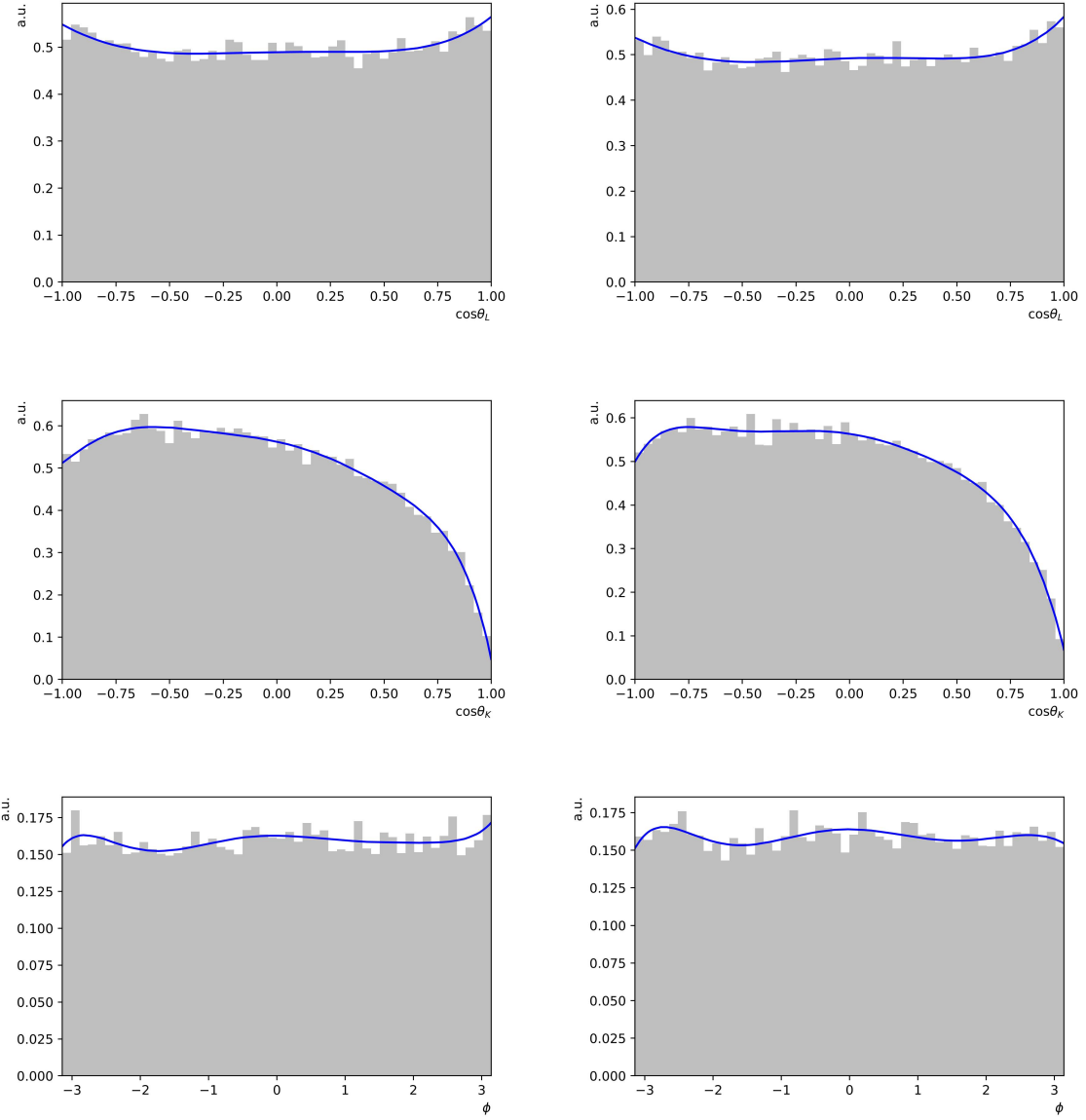


Figure 6: Projections of the three-dimensional acceptance function calculated using  $B^0 \rightarrow K^{*0} e^+ e^-$  phase space MC events into the dimensions of the angles  $\cos \theta_\ell$  (top),  $\cos \theta_K$  (middle),  $\phi$  (bottom) in the trigger categories  $L0E$  (left) and  $L0I$  (right).

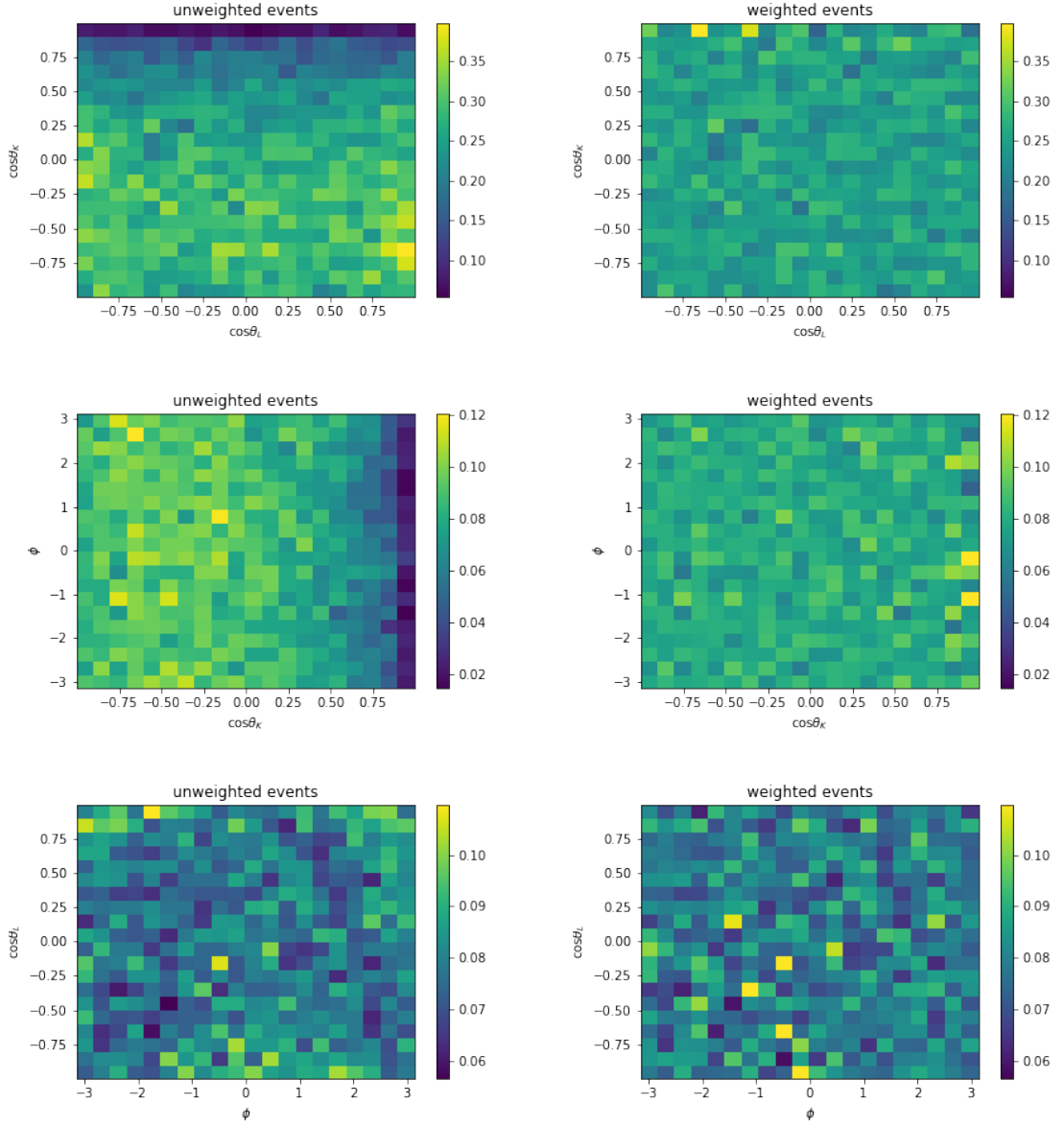


Figure 7: The  $B^0 \rightarrow K^{*0} e^+ e^-$  phase space MC events for the trigger category  $L0E$  used to calculate the acceptance function are shown in two-dimensional histograms with two of the three angles each (left). The distributions are very irregular in comparison to the events reweighted with the inverse detector acceptance (right).

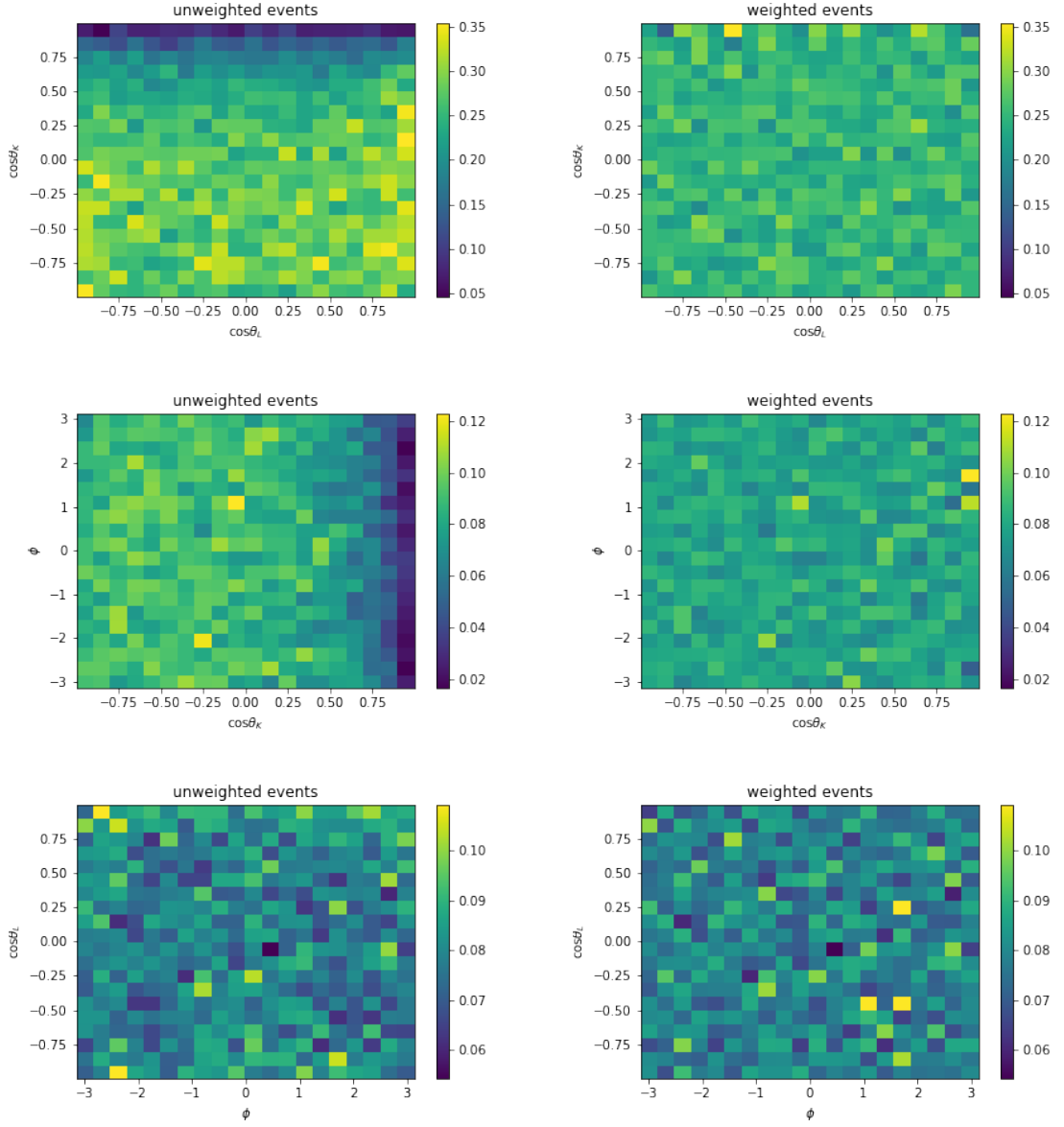


Figure 8: The  $B^0 \rightarrow K^{*0} e^+ e^-$  phase space MC events for the trigger category  $L0I$  used to calculate the acceptance function are shown in two-dimensional histograms with two of the three angles each (left). The distributions are very irregular in comparison to the events reweighted with the inverse detector acceptance (right).

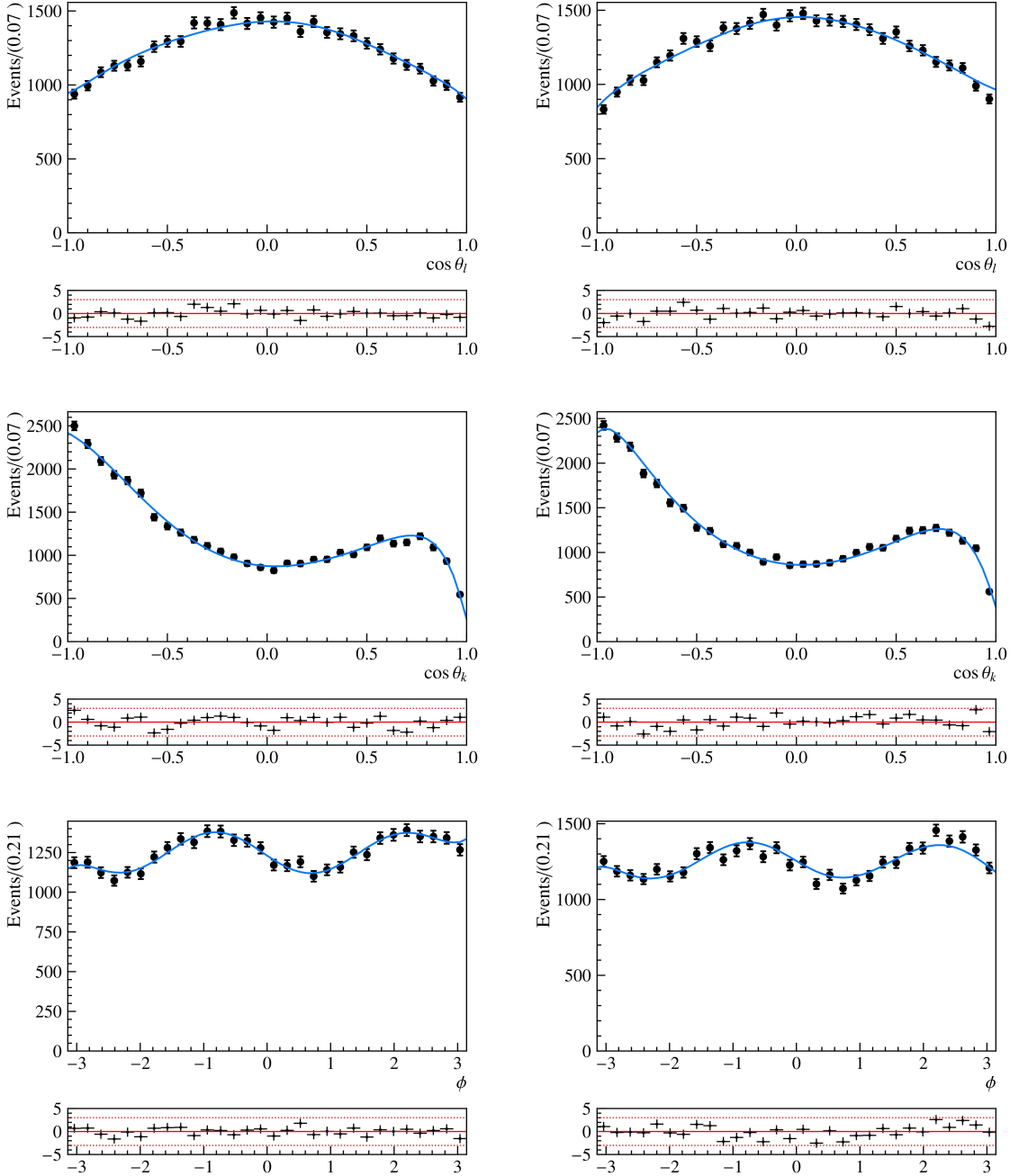


Figure 9: Projections of the three-dimensional angular fit to the  $B^0 \rightarrow K^{*0} J/\psi (\rightarrow e^+ e^-)$  MC simulation into the dimensions of the angles  $\cos \theta_\ell$  (top),  $\cos \theta_K$  (middle),  $\phi$  (bottom) for the trigger categories  $L0E$  (left) and  $L0I$  (right).

### 5.3 Mass Fit

A mass fit is included in the analysis as signal and background events can be better separated using the reconstructed  $B^0$  meson mass than in the angular dimensions. The shape of the  $B^0$  meson mass peak in trigger categories is determined by additionally splitting the simulated  $B^0 \rightarrow K^{*0} J/\psi(\rightarrow e^+e^-)$  events into bremsstrahlungs categories. The three bremsstrahlungs categories *brem0*, *brem1* and *brem2* correspond to 0,1 and 2 bremsstrahlungs photons found in an individual cluster in the ECAL and taken into account to reconstruct the electron energy. The events in bremsstrahlungs categories are fitted individually using an unbinned maximum likelihood fit. The mass shape in the *brem0* category is modelled by a Double Crystal Ball function: [22]

$$DCB(m, \bar{m}, \sigma, \alpha, n) = N \begin{cases} \exp\left(-\frac{(m-\bar{m})^2}{2\sigma^2}\right) & \text{for } \frac{m-\bar{m}}{\sigma} > -\alpha \\ \frac{\left(\frac{n}{\alpha}\right)^n \exp\left(-\frac{1}{2}\alpha^2\right)}{\left(\frac{m-\bar{m}}{\sigma} + \frac{n}{\alpha} - \alpha\right)^n} & \text{for } \frac{m-\bar{m}}{\sigma} \leq -\alpha \end{cases} \quad (5.2)$$

A Double Crystal Ball function with an additional Gaussian function is used for *brem1* and *brem2*. The mass fit results in the three bremsstrahlungs categories for the two trigger categories each are shown in figure 10.

The three bremsstrahlungs categories are combined while taking into account the corresponding fraction of events to yield a single fit function for each trigger category. This process can be tested by fitting the resulting function to the  $B^0 \rightarrow K^{*0} J/\psi(\rightarrow e^+e^-)$  MC simulation for the two trigger categories (shown in figure 11).

### 5.4 Background

The signal selection explained in section 4.1 does not remove all background events from the  $B^0 \rightarrow K^{*0} J/\psi(\rightarrow e^+e^-)$  data, thus a background contribution has to be included in the fit. The background in the mass dimension can be modelled by an exponential function. The angular background can again be modelled using a polynomial expansion with Chebyshev-polynomials.

An angular background fit is done to the background sample obtained for the  $B^0 \rightarrow K^{*0} J/\psi(\rightarrow e^+e^-)$  high-mass side-band with the selection explained in section 4.2. The Chebyshev-polynomials are truncated at order 6 for all three angles. The three-dimensional fit is done using an unbinned maximum likelihood fit. Projections of the background fit into the dimensions of the angles are shown in figure 12.

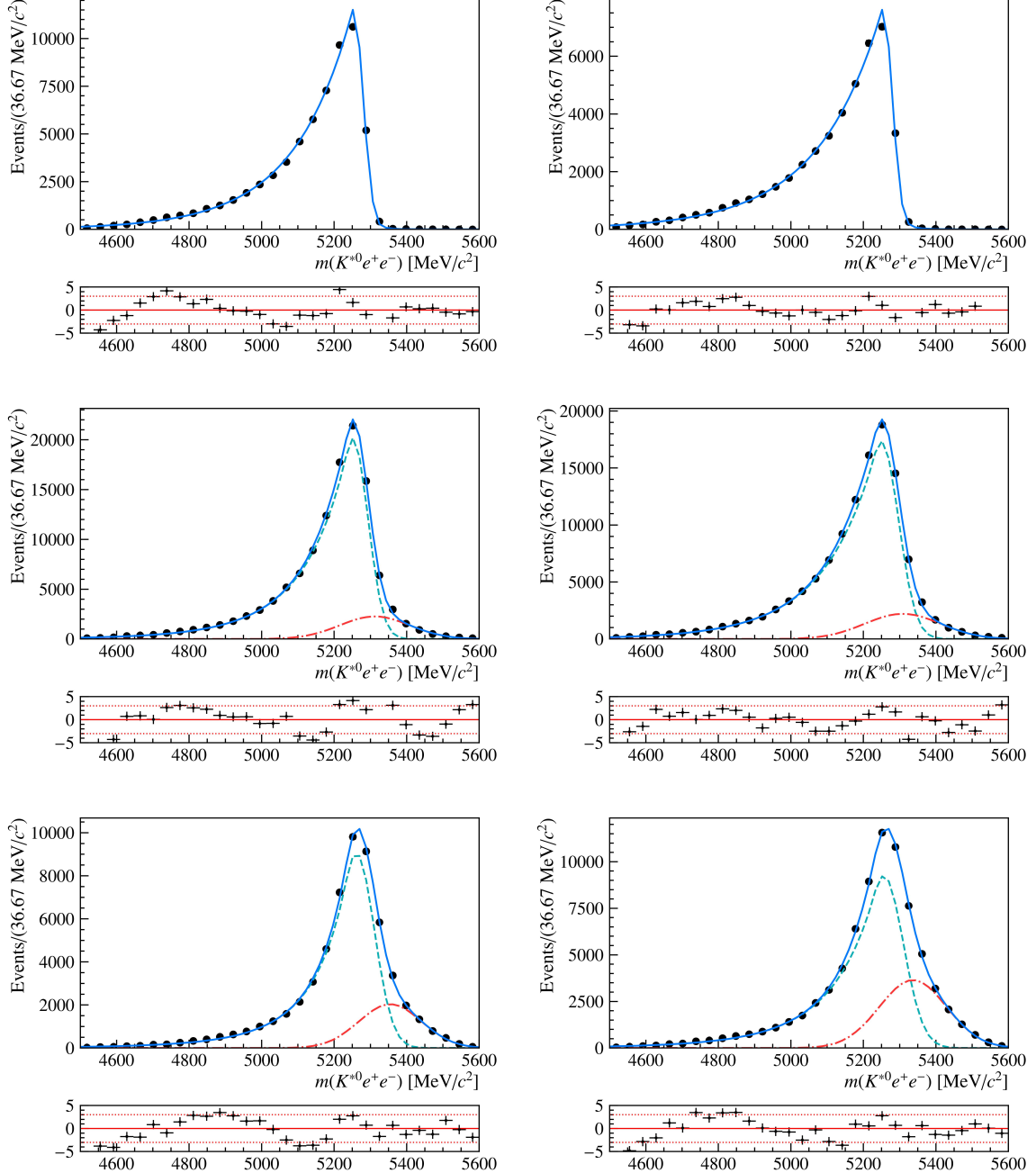


Figure 10: Fit to the  $B^0$  meson mass for  $B^0 \rightarrow K^{*0} J/\psi (\rightarrow e^+e^-)$  MC simulation in the bremsstrahlungs categories *brem0* (top), *brem1* (middle) and *brem2* (bottom) and trigger categories *L0E* (left) and *L0I* (right). The *brem0* categories are fitted with a Double Crystal Ball function while the *brem1* and *brem2* categories are modelled by a Double Crystal Ball function (green) and a Gaussian function (red) which are added to yield the fit function (blue).

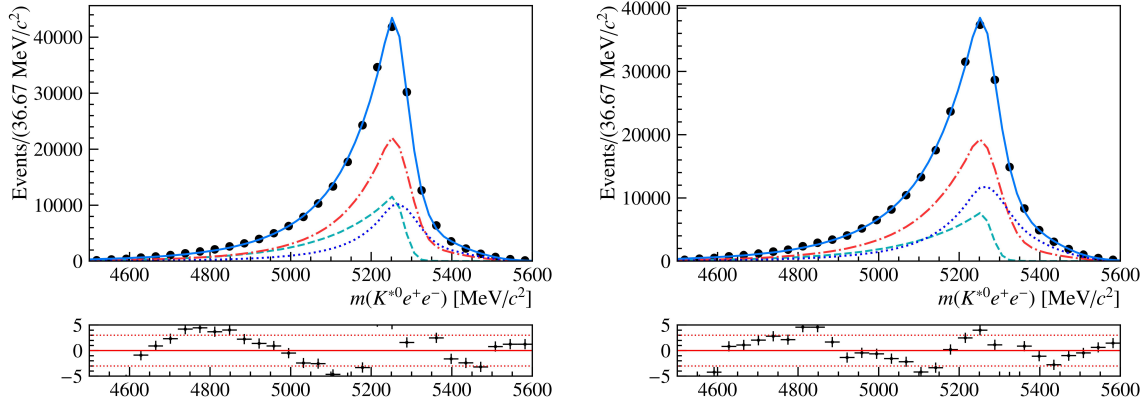


Figure 11: Fit to the  $B^0$  meson mass for  $B^0 \rightarrow K^{*0} J/\psi(\rightarrow e^+e^-)$  MC events in the trigger categories  $L0E$  (left) and  $L0I$  (right). The fit function (blue) is composed of the individual mass fits in bremsstrahlungs categories,  $brem0$  (green),  $brem1$  (red) and  $brem2$  (dark blue).

## 5.5 Four-Dimensional Fit

The three-dimensional angular fit done in section 5.2 and the mass fit from section 5.3 are combined into a four-dimensional fit. For the simulated events a four-dimensional fit should yield the same results as a three-dimensional fit to the angles and a one-dimensional fit to the  $B^0$  meson mass as the simulated events have no background contribution. However, this method helps in separating and fitting the background events in the data as the background events can be easier distinguished by their reconstructed  $B^0$  meson mass than in the angular dimensions.

### 5.5.1 Simulated $B^0 \rightarrow K^{*0} J/\psi(\rightarrow e^+e^-)$ Events

The four-dimensional fit to simulated  $B^0 \rightarrow K^{*0} J/\psi(\rightarrow e^+e^-)$  decays relies on equation 2.4 describing the P-wave signal which is multiplied with the angular acceptance function to yield the angular PDF for the fit in  $\cos\theta_\ell$ ,  $\cos\theta_K$  and  $\phi$ . The mass dimension is modelled by the mass function in trigger categories obtained in section 5.3. The fit is done using an unbinned maximum likelihood fit. Projections of the four-dimensional PDF into the individual dimensions are shown in figure 13 for the trigger category  $L0E$  and figure 14 for the trigger category  $L0I$ . The obtained fit parameters are compared in table 3 and table 4 with the values used in the MC generator from [23].

In general, the MC generator level values are well reproduced. The precision of the fit results is very high and the uncertainties determined in the fit are quite

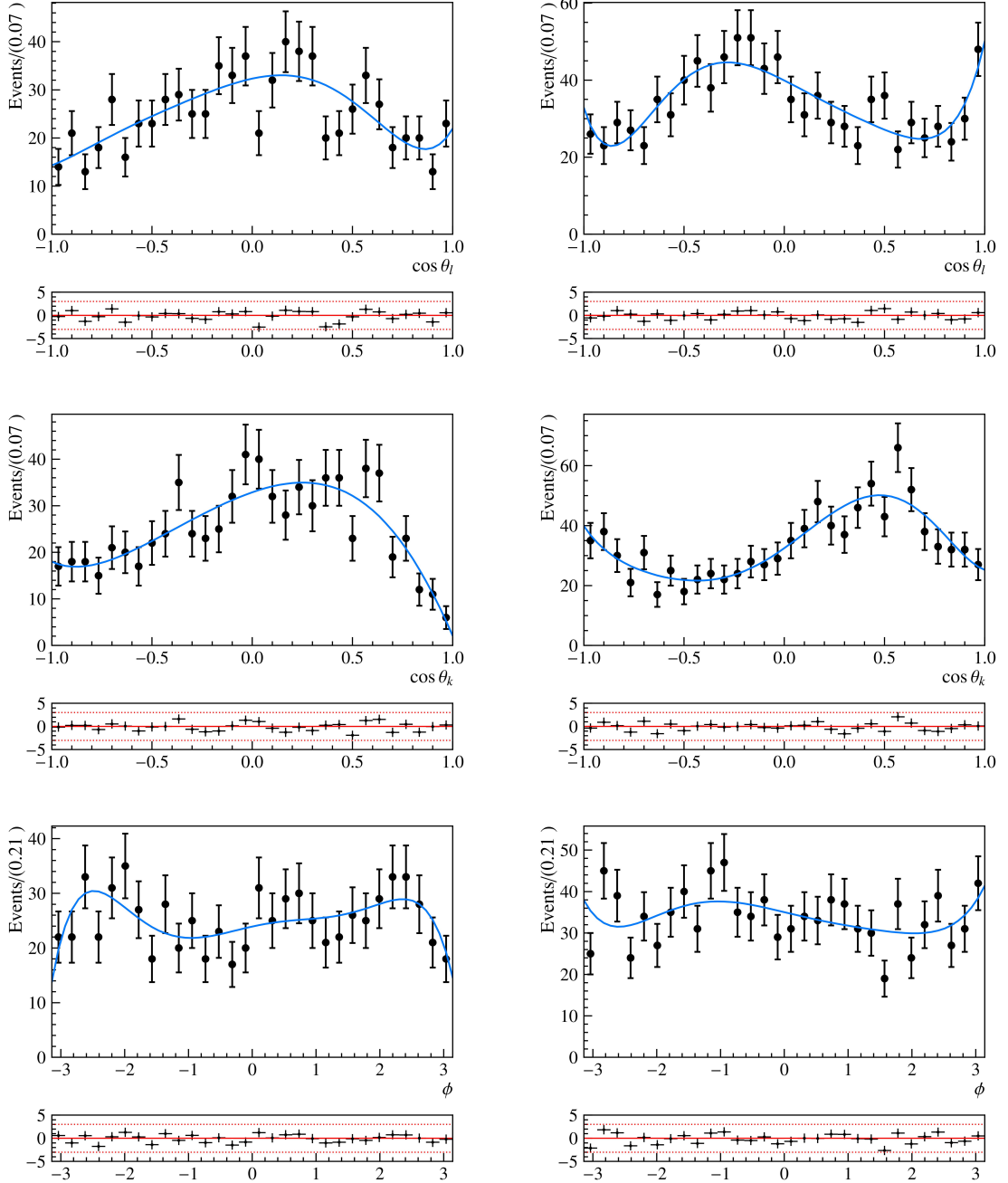


Figure 12: Projections of the three-dimensional background fit to the  $B^0 \rightarrow K^{*0} J/\psi(\rightarrow e^+e^-)$  high-mass side-band sample into the angles  $\cos \theta_\ell$  (top),  $\cos \theta_K$  (middle),  $\phi$  (bottom) for the trigger categories *L0E* (left) and *L0I* (right).

small. Accordingly, the deviations between the fit and the generator level values, while small in absolute terms, are significant when expressed in terms of standard deviations with differences up to  $8\sigma$ . Overall the fit to the MC simulation is able to extract the generator level values suggesting that the event selection and fitting procedures are working properly.

### 5.5.2 Measured $B^0 \rightarrow K^{*0} J/\psi(\rightarrow e^+e^-)$ Events

The angular PDF for the four-dimensional angular fit to  $B^0 \rightarrow K^{*0} J/\psi(\rightarrow e^+e^-)$  data is obtained by multiplying the angular distribution with a P- and S-wave contribution (equation 2.6) with the angular acceptance from section 5.1. The background in each angle is modelled by Chebyshev-polynomials with the order 6. The fit function for the  $B^0$  meson mass is described by the mass function in the two trigger categories obtained in section 5.3. The background in the mass dimension is fitted with an exponential function. The fit uses an unbinned maximum likelihood fit. Projections into the three angles and the  $B^0$  mass are shown in figure 15 for the  $L0E$  events and figure 16 for the  $L0I$  events. Table 5 and table 6 compare the obtained angular observables as well as the S-wave fraction with the the parameters from the angular analysis of the  $B^0 \rightarrow K^{*0} J/\psi(\rightarrow \mu^+\mu^-)$  channel in [10] for which one expects the same values.

Overall, the background contribution to the fit is very low suggesting that the applied event selection is successful in separating the signal events from the background.

The obtained statistical uncertainties are larger than the ones from the fit to the simulated events which corresponds to the larger number of simulated than measured events. However, the uncertainties are smaller than the ones of the observables published for the muon channel. This is partly due to a different number of events used for the fit. Additionally, no systematic uncertainties but only statistical errors were taken into account in this analysis.

The angular observables agree well with the values from the muon channel, the deviations between the electron and muon channel parameters in terms of standard deviations are below  $3\sigma$ . Interestingly, the deviations between the fit results and literature values are higher for the  $L0E$  trigger category than for  $L0I$ , which should be further investigated.

In general, the agreement of the obtained angular parameters with the values published for the muon channel confirms the analysis procedure.

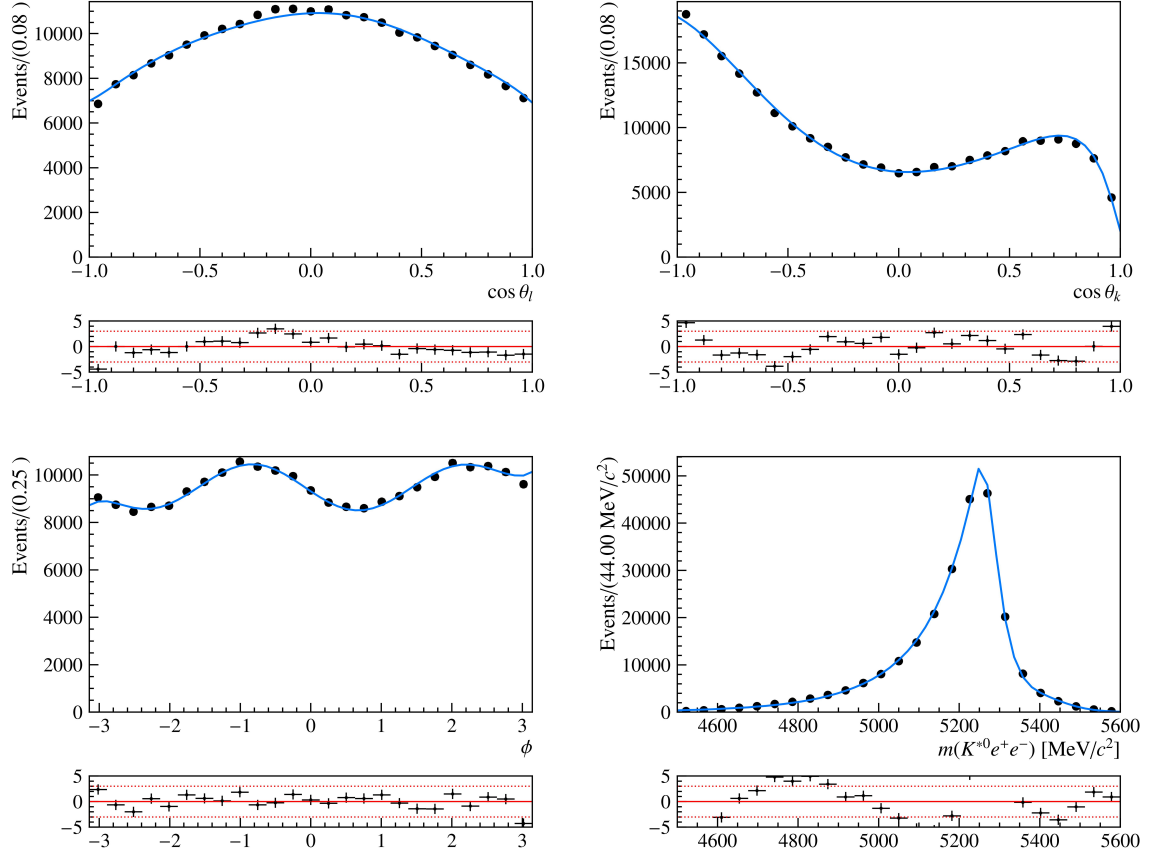


Figure 13: Projections of the four-dimensional angular fit into the dimensions of the angles  $\cos \theta_\ell$  (top left),  $\cos \theta_K$  (top right),  $\phi$  (bottom left) and the  $B^0$  meson mass (bottom right) for  $B^0 \rightarrow K^{*0} J/\psi(\rightarrow e^+e^-)$  MC events in the trigger category  $L0E$ .

Observable	Fit Result	Generator Level MC	Deviation in $\sigma$
$A_{FB}$	$-0.0022 \pm 0.0013$	0.0	-1.7208
$F_L$	$0.6113 \pm 0.0014$	0.6004	7.8587
$S_3$	$-0.0414 \pm 0.0018$	-0.0398	-0.8526
$S_4$	$-0.2218 \pm 0.0021$	-0.2150	-3.2437
$S_5$	$-0.0039 \pm 0.0021$	0.0	-1.8961
$S_7$	$0.0099 \pm 0.0022$	0.0	4.4658
$S_8$	$0.0356 \pm 0.0023$	0.03715	-0.6883
$S_9$	$-0.0888 \pm 0.0018$	-0.0887	-0.0337

Table 3: Angular observables obtained in the four-dimensional angular fit to  $B^0 \rightarrow K^{*0} J/\psi(\rightarrow e^+e^-)$  MC events in the trigger category  $L0E$  compared to the generator level values from [23].

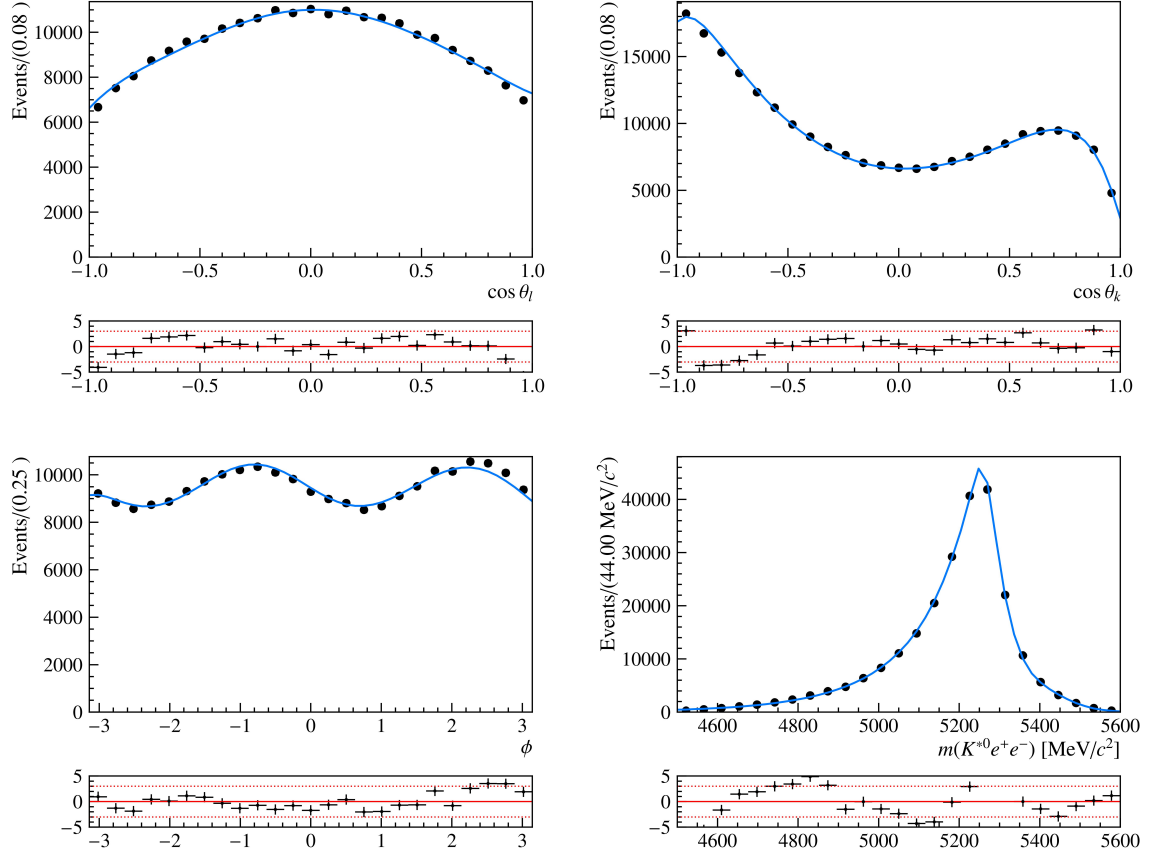


Figure 14: Projections of the four-dimensional angular fit into the dimensions of the angles  $\cos \theta_\ell$  (top left),  $\cos \theta_K$  (top right),  $\phi$  (bottom left) and the  $B^0$  meson mass (bottom right) for  $B^0 \rightarrow K^{*0} J/\psi(\rightarrow e^+e^-)$  MC events in the trigger category  $L0I$ .

Observable	Fit Result	Generator Level MC	Deviation in $\sigma$
$A_{FB}$	$-0.0040 \pm 0.0013$	0.0	-3.1902
$F_L$	$0.6091 \pm 0.0014$	0.6004	6.2520
$S_3$	$-0.0408 \pm 0.0018$	-0.0398	-0.5208
$S_4$	$-0.2234 \pm 0.0021$	-0.2150	-3.9941
$S_5$	$0.0063 \pm 0.0021$	0.0	3.0351
$S_7$	$0.0103 \pm 0.0022$	0.0	4.6469
$S_8$	$0.0367 \pm 0.0023$	0.03715	-0.1863
$S_9$	$-0.0852 \pm 0.0018$	-0.0887	1.9554

Table 4: Angular observables obtained in the four-dimensional angular fit to  $B^0 \rightarrow K^{*0} J/\psi(\rightarrow e^+e^-)$  MC events in the trigger category  $L0I$  compared to the generator level values from [23].

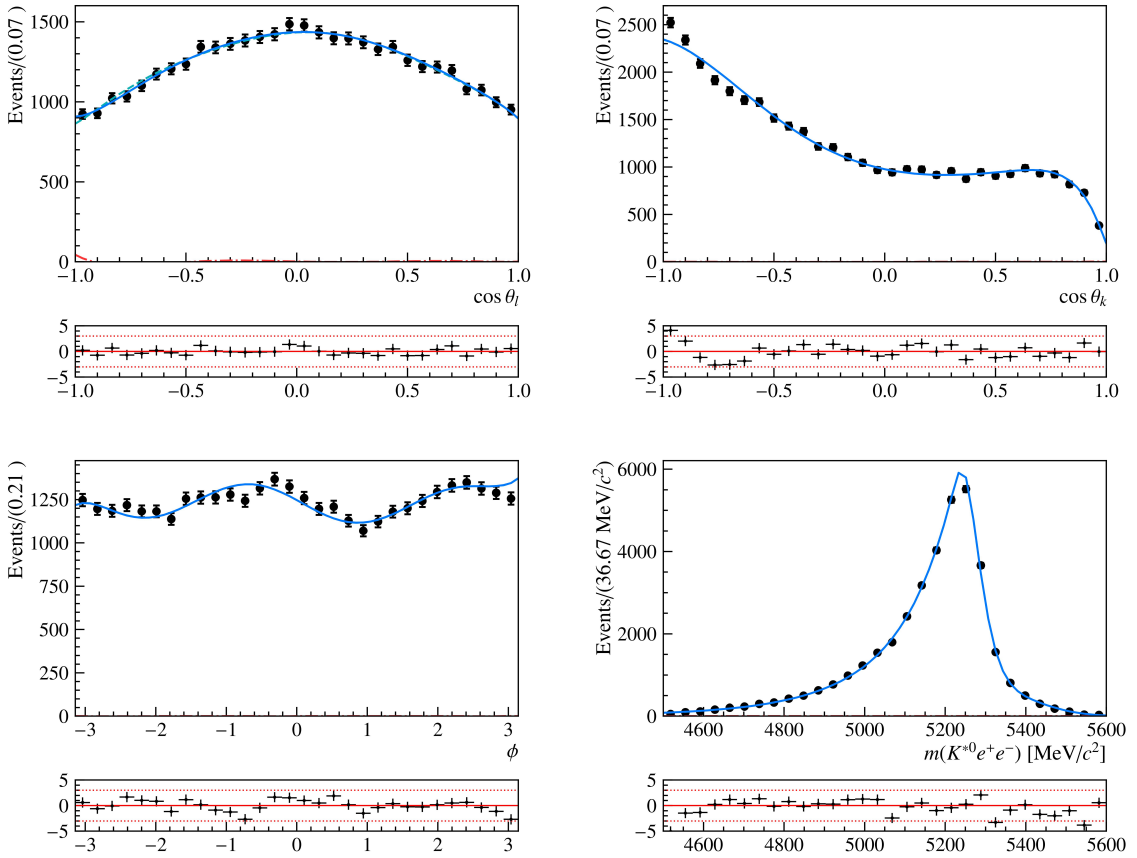


Figure 15: Projections of the four-dimensional angular fit into the dimensions of the angles  $\cos \theta_\ell$  (top left),  $\cos \theta_K$  (top right),  $\phi$  (bottom left) and the  $B^0$  meson mass (bottom right) for  $B^0 \rightarrow K^{*0} J/\psi(\rightarrow e^+e^-)$  data events in the trigger category  $L0E$ . The signal (green) and background (red) events are modelled individually and added to yield the fit function (blue).

Observable	Fit Result	Observables measured in $B^0 \rightarrow K^{*0} J/\psi(\rightarrow \mu^+\mu^-)$	Deviation in $\sigma$
$A_{FB}$	$0.005 \pm 0.004$	$0.0 \pm 0$	1.4881
$F_L$	$0.563 \pm 0.004$	$0.572 \pm 0.009$	-0.9500
$S_3$	$-0.005 \pm 0.006$	$-0.013 \pm 0.010$	0.6862
$S_4$	$-0.254 \pm 0.006$	$-0.249 \pm 0.006$	-0.5558
$S_5$	$-0.004 \pm 0.006$	$0.0 \pm 0$	-0.5937
$S_7$	$0.017 \pm 0.006$	$0.0 \pm 0$	2.7284
$S_8$	$-0.061 \pm 0.006$	$-0.048 \pm 0.007$	-1.3822
$S_9$	$-0.086 \pm 0.006$	$-0.084 \pm 0.006$	-0.2818
$F_S$	$0.103 \pm 0.009$	$0.084 \pm 0.010$	1.3921

Table 5: Angular observables obtained in the four-dimensional fit to  $B^0 \rightarrow K^{*0} J/\psi(\rightarrow e^+e^-)$  data events in the trigger category  $L0E$  compared to the parameters published for the  $B^0 \rightarrow K^{*0} J/\psi(\rightarrow \mu^+\mu^-)$  channel in [10].

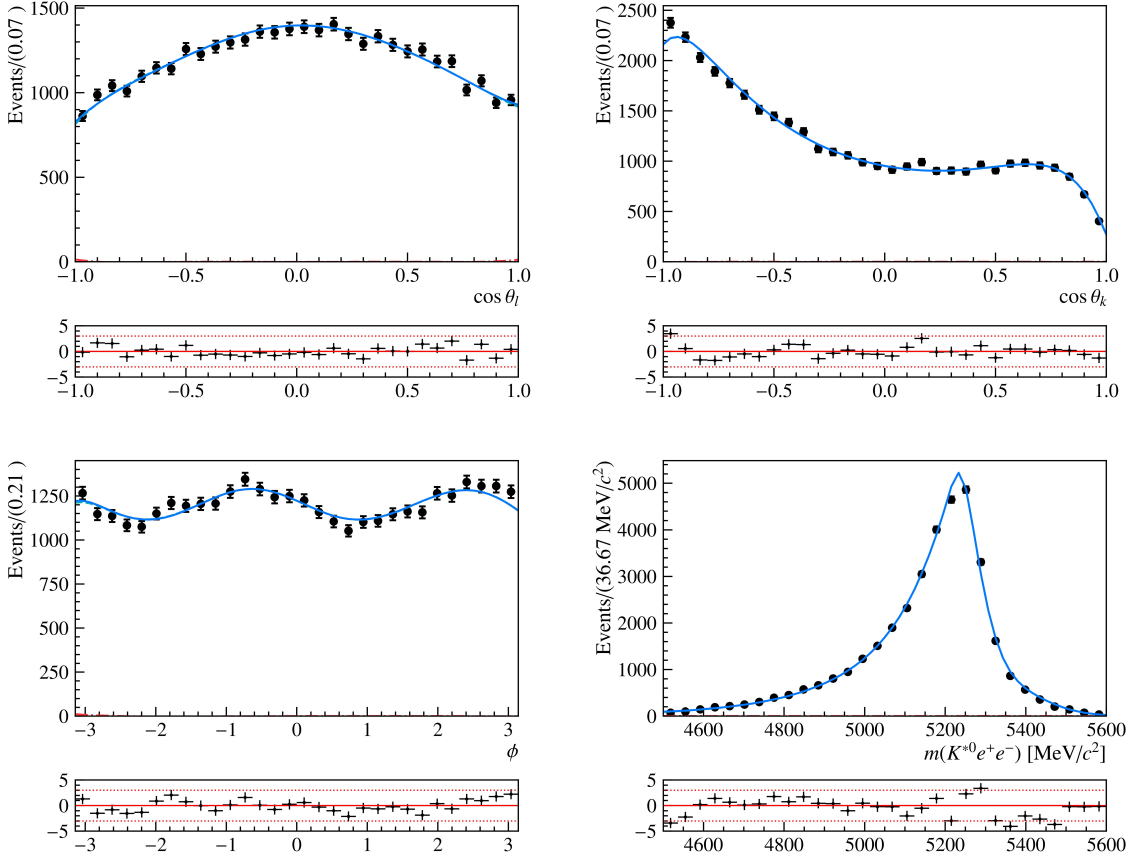


Figure 16: Projections of the four-dimensional angular fit into the dimensions of the angles  $\cos \theta_\ell$  (top left),  $\cos \theta_K$  (top right),  $\phi$  (bottom left) and the  $B^0$  meson mass (bottom right) for  $B^0 \rightarrow K^{*0} J/\psi(\rightarrow e^+e^-)$  data events in the trigger category  $L0I$ . The signal (green) and background (red) events are modelled individually and added to yield the fit function (blue).

Observable	Fit Result	Observables measured in $B^0 \rightarrow K^{*0} J/\psi(\rightarrow \mu^+\mu^-)$	Deviation in $\sigma$
$A_{FB}$	$-0.001 \pm 0.004$	$0.0 \pm 0$	-0.2149
$F_L$	$0.559 \pm 0.004$	$0.572 \pm 0.009$	-1.3565
$S_3$	$-0.010 \pm 0.006$	$-0.013 \pm 0.010$	0.2931
$S_4$	$-0.254 \pm 0.006$	$-0.249 \pm 0.006$	-0.63848
$S_5$	$0.000 \pm 0.006$	$0.0 \pm 0$	0.0090
$S_7$	$-0.004 \pm 0.006$	$0.0 \pm 0$	-0.6866
$S_8$	$-0.051 \pm 0.006$	$-0.048 \pm 0.007$	-0.2742
$S_9$	$-0.079 \pm 0.006$	$-0.084 \pm 0.006$	0.6056
$F_S$	$0.094 \pm 0.009$	$0.084 \pm 0.010$	0.7732

Table 6: Angular observables obtained in the four-dimensional fit to  $B^0 \rightarrow K^{*0} J/\psi(\rightarrow e^+e^-)$  data events in the trigger category  $L0I$  compared to the parameters published for the  $B^0 \rightarrow K^{*0} J/\psi(\rightarrow \mu^+\mu^-)$  channel in [10].

## 6 Conclusion

The goal of this thesis is to perform an angular analysis to  $B^0 \rightarrow K^{*0}J/\psi(\rightarrow e^+e^-)$  through a four-dimensional fit to the three decay angles  $\cos\theta_\ell$ ,  $\cos\theta_K$  and  $\phi$  and the  $B^0$  meson mass. The fit was done in two trigger categories and included the detector acceptance as well as a fit to the background for the data events. For simulated  $B^0 \rightarrow K^{*0}J/\psi(\rightarrow e^+e^-)$  events the analysis returns the observable values used to generate the MC simulation while the fit to the 2016 data yields values that are in good agreement to the angular observables measured for the muon channel  $B^0 \rightarrow K^{*0}J/\psi(\rightarrow \mu^+\mu^-)$  in [10]. The results can serve as a reference for the angular analysis of the rare decay  $B^0 \rightarrow K^{*0}e^+e^-$ .

This work can be continued by evaluating the systematic uncertainties influencing the fit results which have not been evaluated as only statistical uncertainties were considered. For example, a systematic uncertainty stems from the form of the angular acceptance function, in particular the orders of the Legendre-polynomials used. Similarly, the orders of the Chebyshev-polynomials used to model the angular background result in a systematic uncertainty. However since the contribution of the background to the data fit is very small the effect can probably be neglected. Further investigations are also required for the differences seen between the two trigger categories in the data fit. One starting point would be to include weights to correct for differences in the MC simulation and data for the trigger categories which do not have to be well represented in the MC events.

## Bibliography

- [1] Mark Thomson. *Modern Particle Physics*. Cambridge University Press, Sept. 2013. DOI: [10.1017/cbo9781139525367](https://doi.org/10.1017/cbo9781139525367).
- [2] Simone Bifani et al. “Review of lepton universality tests in B decays”. In: *Journal of Physics G: Nuclear and Particle Physics* 46.2 (Dec. 2018). DOI: [10.1088/1361-6471/aaf5de](https://doi.org/10.1088/1361-6471/aaf5de).
- [3] The LHCb Collaboration. “Angular analysis of the  $B^0 \rightarrow K^{*0}e^+e^-$  decay in the low-q2 region”. In: *Journal of High Energy Physics* 2015.4 (Apr. 2015). DOI: [10.1007/jhep04\(2015\)064](https://doi.org/10.1007/jhep04(2015)064).
- [4] The LHCb Collaboration. “Differential branching fraction and angular analysis of the decay  $B^0 \rightarrow K^{*0}\mu^+\mu^-$ ”. In: *Journal of High Energy Physics* 2013.8 (Aug. 2013). DOI: [10.1007/jhep08\(2013\)131](https://doi.org/10.1007/jhep08(2013)131).
- [5] The LHCb Collaboration. “Angular analysis of the  $B^0 \rightarrow K^{*0}\mu^+\mu^-$  decay using 3 fb-1 of integrated luminosity”. In: *Journal of High Energy Physics* 2016.2 (Feb. 2016). DOI: [10.1007/jhep02\(2016\)104](https://doi.org/10.1007/jhep02(2016)104).
- [6] The LHCb Collaboration. “Test of lepton universality with  $B^0 \rightarrow K^{*0}\ell^+\ell^-$  decays”. In: *Journal of High Energy Physics* 2017.08 (Aug. 2017). DOI: [10.1007/jhep08\(2017\)055](https://doi.org/10.1007/jhep08(2017)055).
- [7] Wolfgang Demtröder. *Experimentalphysik 4: Kern-, Teilchen- und Astrophysik*. Springer, 2010. DOI: [10.1007/978-3-642-01598-4](https://doi.org/10.1007/978-3-642-01598-4).
- [8] Particle Data Group. “Review of Particle Physics”. In: *Progress of Theoretical and Experimental Physics* 2020.8 (Aug. 2020). DOI: [10.1093/ptep/ptaa104](https://doi.org/10.1093/ptep/ptaa104).
- [9] Wolfgang Altmannshofer et al. “Symmetries and asymmetries of  $B \rightarrow K^*\mu^+\mu^-$  decays in the Standard Model and beyond”. In: *Journal of High Energy Physics* 2009.01 (Jan. 2009). DOI: [10.1088/1126-6708/2009/01/019](https://doi.org/10.1088/1126-6708/2009/01/019).
- [10] The LHCb Collaboration. “Measurement of the polarization amplitudes in  $B \rightarrow J/\psi K^*(892)^0$  decays”. In: *Physical Review D* 88.5 (Sept. 2013). DOI: [10.1103/physrevd.88.052002](https://doi.org/10.1103/physrevd.88.052002).
- [11] Lyndon Evans et al. “LHC Machine”. In: *Journal of Instrumentation* 3.08 (Aug. 2008). DOI: [10.1088/1748-0221/3/08/s08001](https://doi.org/10.1088/1748-0221/3/08/s08001).
- [12] Stephan Eisenhardt. “The LHCb Upgrade”. In: *Journal of Physics: Conference Series* 447 (July 2013). DOI: [10.1088/1742-6596/447/1/012046](https://doi.org/10.1088/1742-6596/447/1/012046).

- [13] The LHCb Collaboration. “Design and performance of the LHCb trigger and full real-time reconstruction in Run 2 of the LHC”. In: *Journal of Instrumentation* 14.04 (Apr. 2019). doi: 10.1088/1748-0221/14/04/p04013.
- [14] Concezio Bozzi et al. “The LHCb software and computing upgrade for Run 3: opportunities and challenges”. In: *Journal of Physics: Conference Series* 898 (2017). doi: 10.1088/1742-6596/898/11/112002.
- [15] The LHCb Collaboration. “The LHCb Detector at the LHC”. In: *Journal of Instrumentation* 3.08 (Aug. 2008). doi: 10.1088/1748-0221/3/08/s08005.
- [16] Chris Burr et al. *The LHCb Starterkit lessons*. 2020. URL: <https://lhcb.github.io/starterkit-lessons/>.
- [17] Martino Borsato et al. “Angular analysis of  $B^0 \rightarrow K^{*0} e^+ e^-$  at very low  $q^2$  at LHCb”. In: (Oct. 2020). URL: <https://cds.cern.ch/record/2713167/>.
- [18] Patrick Koppenburg et al. *StrippingBu2LLK<sub>e</sub>eLine2*. 2020. URL: [http://lhcbdoc.web.cern.ch/lhcbdoc/stripping/config/stripping28r1p1/leptonic/strippingbu2llk\\_eeline2.html](http://lhcbdoc.web.cern.ch/lhcbdoc/stripping/config/stripping28r1p1/leptonic/strippingbu2llk_eeline2.html).
- [19] Zhenzi Wang. *Samples And Selection*. 2020. URL: [https://gitlab.cern.ch/LHCb-RD/ewp-bd2ksteeangular-legacy/-/tree/master/samples\\_and\\_selection](https://gitlab.cern.ch/LHCb-RD/ewp-bd2ksteeangular-legacy/-/tree/master/samples_and_selection).
- [20] Zhenzi Wang. *Instructions for the usage of combinatorial MVA scripts*. 2020. URL: [https://gitlab.cern.ch/LHCb-RD/ewp-bd2ksteeangular-legacy/-/tree/master/samples\\_and\\_selection/Comb\\_MVA](https://gitlab.cern.ch/LHCb-RD/ewp-bd2ksteeangular-legacy/-/tree/master/samples_and_selection/Comb_MVA).
- [21] Maxime Schubinger et al.  $B^0 \rightarrow K^{*0} \ell^+ \ell^-$  angular analysis. 2021. URL: <https://gitlab.cern.ch/LHCb-RD/ewp-bd2ksteeangular-legacy/>.
- [22] Andrea Mauri. *pdfs.py*. 2020. URL: <https://gitlab.cern.ch/LHCb-RD/ewp-bd2ksteeangular-legacy/-/blob/master/b2kstll/b2kstll/models/pdfs.py>.
- [23] Patrick Robbe. *Bd\_JpsiKst,ee=DecProdCut.dec*. 2012. URL: [https://gitlab.cern.ch/lhcb-datapkg/Gen/DecFiles/-/blob/v30r52/dkfiles/Bd\\_JpsiKst,ee=DecProdCut.dec](https://gitlab.cern.ch/lhcb-datapkg/Gen/DecFiles/-/blob/v30r52/dkfiles/Bd_JpsiKst,ee=DecProdCut.dec).

## Acknowledgements

I would like to thank Professor Dr. Ulrich Uwer for allowing me to write my Bachelor thesis in his group. Many thanks to Dr. Martino Borsato for supervising this thesis and to Fabian Glaser! A huge thanks to my family and friends!

## Declaration

I declare that I have written this thesis by myself and used no other sources or aids than those indicated.

Ottendorf-Okrilla, 09.04.2021

*Celine Biner*